OPTICA

Beam deflection and negative drag in a moving nonlinear medium

Ryan Hogan,[1,*] Akbar Safari,[1] Giulia Marcucci,[1] Boris Braverman,[1] and Robert W. Boyd[1,2]

[1]Department of Physics, University of Ottawa, Ottawa, Ontario K1N 6N5, Canada
[2]Institute of Optics, University of Rochester, Rochester, New York 14627, USA
*rhoga054@uottawa.ca

Received 20 September 2022; revised 16 March 2023; accepted 3 April 2023; published 24 April 2023

Light propagating in a moving medium is subject to light drag. While the light drag effect due to the linear refractive index is often negligibly small, the light drag can be enhanced in materials with a large group index. Here we show that the nonlinear refractive index can also play a crucial role in the propagation of light in moving media and results in a beam deflection. We perform an experiment with a rotating ruby crystal that exhibits a very large negative group index and a positive nonlinear refractive index. The negative group index drags the light opposite to the motion of the medium. However, the positive nonlinear refractive index deflects the beam along with the motion of the medium and hinders the observation of the negative drag effect. Hence, we show that it is necessary to measure not only the transverse shift of the beam but also its output angle to discriminate the light drag effect from beam deflection. Our work provides insight into applications for all-optical control of light trajectories, particularly for beam steering, mode sorting, and velocimetry.

https://doi.org/10.1364/OPTICA.476094

1. INTRODUCTION

Propagation of light in moving media has been studied for more than two centuries [1–11]. Upon propagation, the trajectory of light can be manipulated through self-action effects [12,13], beam deflection [14,15], photon-drag [16–18], and many other phenomena. The photon-drag effect was hypothesized by Fresnel [1], and then experimentally observed by Fizeau [2]. Fizeau's landmark experiment measured the shift of interference fringes within an interferometer containing a tube with moving water. These shifts in the fringes supported the idea that light is dragged in moving media. This phenomenon has gained increasing interest in the field of optics and is indeed still investigated in modern day research [6,7,10,19–23].

Photon-drag can be longitudinal or transverse, i.e., along or perpendicular to the light propagation direction, respectively. This paper focuses on transverse photon-drag [24], distinctly different from longitudinal drag [25]. Figure 1(a) sketches the light propagation in a medium of length L in two cases: (i) a stationary medium and (ii) a medium moving transversely at speed v in which the output light is subject to a transverse shift given by

$$\Delta y = \frac{v}{c}\left(n_g - \frac{1}{n_\phi}\right) L, \tag{1}$$

with c the speed of light in vacuum, and n_g and n_ϕ the group and phase indices, respectively.

Typically phase and group indices are not large, and therefore do not create large transverse shifts. Recent studies show larger shifts using slow light media (i.e., large group indices) [11,23,25,26]. Group indices as large as $n_g = 10^6$ are often achieved through nonlinear phenomena such as coherent population oscillation (CPO) [27] or electromagnetically induced transparency (EIT) [28]. Therefore, utilizing these effects can significantly boost the photon-drag effect, or allow negative photon-drag [29].

Although some nonlinear phenomena, such as EIT and CPO, can enhance the group index, the presence of an intense beam invites other nonlinear responses, specifically Kerr-type nonlinearities that will also contribute a deflection to the measurement. In the presence of a strong saturating beam, one must consider nonlinear deflection in a moving medium, which can be larger than and confused with the photon-drag effect. While the enhanced photon-drag effect depends on the group index including any nonlinear contribution [see Eq. (1)], the nonlinear deflection depends on the nonlinear refractive index of the medium. Thus, it seems that one should be able to achieve a large enhancement in the drag effect with negligible nonlinear deflection. However, according to the Kramers–Kronig relation, a large group index often is associated with a sluggish response [30]. Therefore, if the large group index is achieved through a nonlinear interaction, one has to be careful with the nonlinear deflection and measure the output angle, a critical step missing in previous works [26,31,32].

In this paper, we use a rotating ruby rod to study the nonlinear light propagation in a moving medium. To reach high speeds in a solid material, rotation is more feasible experimentally than linear motion. Consider a beam incident on the medium at a distance

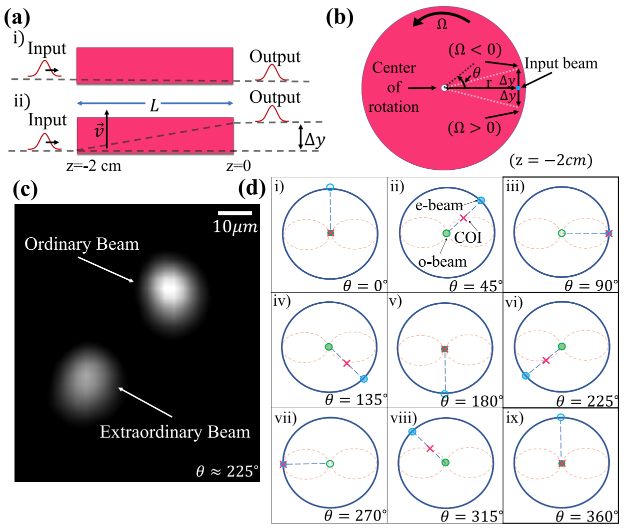

Fig. 1. (a) Schematic showing laser beam propagation in (i) a stationary medium versus (ii) a moving medium that exhibits a transverse shift of Δy. For simplicity of illustration, we show the laser beams as pulses. (b) The edge of a rotary ruby rod is used to achieve an approximately linear motion in the $-y$ ($+y$) direction when the crystal rotates clockwise (counterclockwise). (c) Single frame imaged at the input face of the crystal ($z = -2$ cm) showing o- and e-beams propagated through the 2 cm long ruby crystal. (d) Diagram showing the trajectories of o- and e-beams at different crystal orientations highlighting the change in intensity of each beam at 45 deg intervals. The red "x" shows the center of intensity (COI) position for different crystal orientations highlighting the emergence of a figure-eight-like pattern, while o- and e-beams are shown by green and blue dots, respectively, with varying transparency to signify their relative intensities.

r from the center of rotation [Fig. 1(b)], and using a slow light medium with $n_g \gg 1/n_\phi$; the transverse drag can be simplified to

$$\Delta y \approx n_g L \left(\frac{r\Omega}{c}\right), \tag{2}$$

where Ω is the medium's rotational speed, and the medium radius is r.

Similar to alexandrite [27], a recent study shows that ruby exhibits an extremely large negative group index ($n_g \approx -10^6$) at large laser intensities at 473 nm wavelength [26,33]. Hence, according to Eq. (2), one expects to observe a large negative photon-drag effect in which the position of the beam shifts in the direction opposite to the motion of the medium.

Nevertheless, since ruby also exhibits nonlinear refraction, the beam deflects toward the direction motion of the medium due to nonlinear deflection. Furthermore, the birefringence of the crystal splits the input beam into ordinary (o) and extraordinary (e) beams that separate upon propagation in the crystal. The e-beam revolves with the rotation of the ruby rod. Moreover, the propagations of o- and e-beams are coupled through the nonlinear interaction in ruby, which creates an attractive force between beams and further complicates their trajectory. We study the trajectories of these beams experimentally and simulate the propagation using nonlinear Schrodinger equations. Due to the simultaneous presence of birefringence, intensity-dependent photon-drag, and strong nonlinearity, ruby can serve as a solid-state platform rich in physics with potential applications to beam steering [34,35], polarization detection [36,37], image rotation [26,32], velocimetry [38], and potential for solitonic behavior with associated applications [39–41].

2. METHODS

The laser source used in the experiment, as shown in Fig. 2, is a continuous-wave (CW) diode-pumped solid-state laser operating at 473 nm with an output power of 520 mW. We control the power of the laser beam using a half-wave plate and polarizing beam splitter. We use a 2 cm long ruby rod, 9 mm in diameter, with a Cr^{3+} doping concentration of 5%. We focus the laser beam onto the input face of the crystal near the edge (0.1 mm away) far from the center of rotation ($r = 0.35$ mm). The ruby was mounted in a hollow spindle whose rotation was controlled by a stepper motor and belt. The output face of the crystal was imaged onto a CCD camera using a 4-f lens system.

When linearly polarized light is shined onto the rotating birefringent medium, the light sees two refractive indices upon propagation, $n_o = 1.770$ and $n_e = 1.762$. Without any influence of nonlinearity or photon-drag, the two beams (o- and e-) then propagate with a finite angular separation of $\gamma_b = 8$ mrad, known as a birefringent walk-off. The relative beam intensity reaches maxima and minima each quarter turn of the crystal (i.e., every 90 deg).

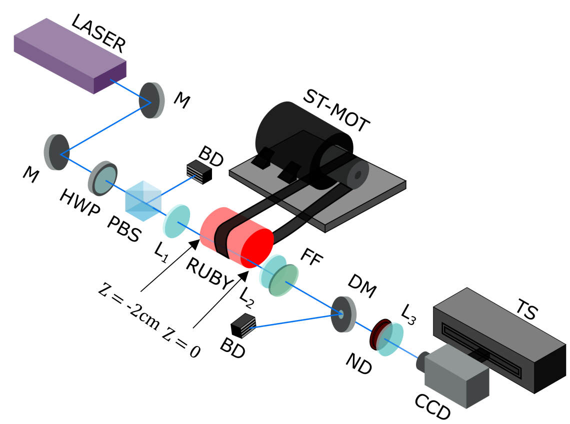

Fig. 2. 520 mW continuous-wave laser beam at 473 nm is focused using a 100 mm focal length plano–convex lens L_1 to a spot size of 20 μm onto the input face of rotating ruby rod. The rod spins around its axis driven by a stepper motor. The laser beam at the output of the crystal is imaged onto a CCD camera with unity magnification using a 4-f system consisting of two lenses L_2 and L_3 of focal length $f = 150$ mm. The CCD camera captures the beam, with a frame rate of 1000 fps, as the stepper motor is rotated at various speeds. An ND filter is placed between the dielectric mirror and lens 2, L_2, for nonlinear measurements, and between L_1 and the ruby for linear measurements. The CCD camera images at different z positions using a translation stage. Measurements are taken at $z = 0$, $z = 0.762$, and $z = 1.524$ cm to measure the transverse shift, as well as the output angle of the beam as it exits the crystal. The fluorescence filter FF (high transmission near 473 nm) is used to minimize fluorescence. The dielectric mirror DM is used as a neutral density filter with low absorption to limit the beam intensity for high-power tests, while also minimizing image distortions due to aberrations induced by thermal nonlinearities in a standard neutral density filter. Input beam power was controlled by a half-wave plate and a polarizing beam splitter before the ruby crystal. M, mirror; HWP, half-wave plate; PBS, polarizing beam splitter; BD, beam dump; L_1, plano–convex lens [f = 100 mm]; L_2, plano–convex lens [f = 150 mm]; L_3, plano-convex lens [f = 150 mm]; FF, fluorescence filter; DM, dielectric mirror; ND, neutral density filter [O.D. 1]; CCD, charge-coupled device.

The beam input is aligned such that, regardless of crystal orientation, the o-beam propagates directly through the crystal, while the e-beam revolves around the o-beam. When imaging the input face of the crystal onto the camera, the o- and e-beams appear distinctly on the image [Fig. 1(c)]. However, they diffract and overlap upon propagation and become indistinguishable at the output of the crystal, where the transverse shifts are measured. Therefore, we use the center of intensity (COI) of the output light, represented as a red "x" in Fig. 1(d), to track the motion of the average position of the laser beam.

3. RESULTS

We measure the COI at $z = 0$ for three input powers of 0.2, 100, and 520 mW and rotational speeds of $\Omega = \pm 50, \pm 100, \pm 1000$, and ± 9000 deg/s in clockwise (negative) and counterclockwise (positive) directions. Figure 3 shows the COI trajectories for an input laser power of 0.2 mW, considered as the linear regime. We observe that all speeds trace out figure-eight-like trajectories and do not show a transverse shift. The figure-eight trajectory is a result of the e-beam revolving around the o-beam in the rotating crystal. Note that in the linear regime, the group index is of the order of unity, and the transverse drag effect is negligibly small.

Figure 4 shows the COI trajectories in the nonlinear regime. At low speeds ($\Omega \leq 100$ deg/s), the o- and e- beams couple to each other causing significant variation in the traces of the COI upon rotation. At high speeds, the deviations from a figure-eight-like pattern start to average out and resemble those of the linear results. However, in contrast to the linear regime, a transverse shift in the COI is very clear.

The deviations from a figure-eight pattern are more apparent in the highly nonlinear regime (Fig. 5) and where the trajectories are noisier and do not average out at high speeds. This noise is likely due to a large thermal effect that locally affects the beam frame by frame. With lower speeds, we observe that the figure-eight-like COI trajectories knot near the center as a result of the nonlinear coupling of o- and e- beams. Simulations are compared showing agreement in the traced patterns, and magnitudes of the transverse shift. A noticeable discrepancy between measurements and simulations is that the experimental trajectories do not close near the center of the figure-eight. We attribute this disagreement to the assumption that rotational movement is approximately translational along the y direction. However, the beam is not infinitely far from the center of rotation and therefore would experience a small amount of drag in the x direction. Another reason might arise from the imperfect H polarization caused by the optical elements. Moreover, if the crystal faces are slightly non-parallel, this also could cause a difference in the output angle of the light depending on the crystal orientation in addition to the birefringence effects.

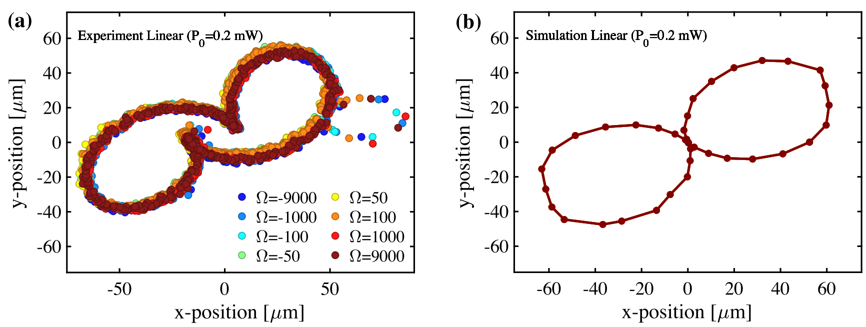

Fig. 3. (a) Experimentally measured COI trajectories in the linear regime. (b) Simulated COI trajectories in the linear regime. The color scheme of the legend in (a) is the same for the simulated curves shown in (b). COI trajectories are plotted for rotation speeds of $\Omega = \pm 50, \pm 100, \pm 1000$, and ± 9000 deg/s. Here, clockwise and counterclockwise rotation (looking into the beam) correspond to positive and negative rotation speeds, respectively. There is not any significant shift between the figure-eight-like trajectories at different speeds, as the group index and nonlinear refraction are negligibly small in the linear regime. The figure-eight-like pattern does not close in the center for the experimental results due to the polarization impurity of incident light in the low-power regime.

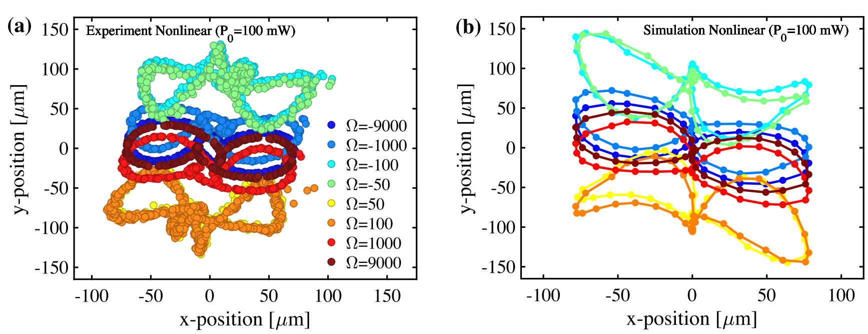

Fig. 4. (a) Experimentally measured and (b) simulated COI trajectories in the nonlinear regime (input laser power of 100 mW). COI trajectories of o- and e- beams [schematically shown in Fig. 1(d)] are plotted for an input laser power of 100 mW, considered as the nonlinear regime for different rotational speeds (Ω) in units of deg/s. At low speeds, o- and e-beams couple to each other, causing significant variation in the traces of the COI upon rotation. Therefore, these patterns are different from the figure-eight-like patterns seen in the linear regime. At high speeds, the deviations from a figure-eight pattern start to average out. All that remains in the high-speed limit is that the figure-eight patterns are shifted from one another for positive and negative rotation speeds as a result of nonlinear deflection.

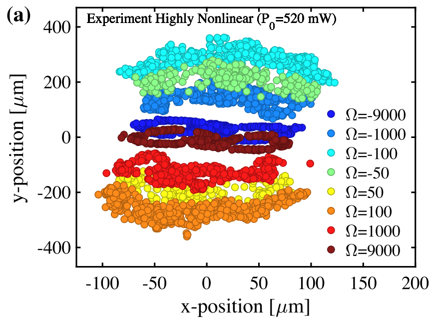

Fig. 5. (a) Experimentally measured and (b) simulated COI trajectories in the nonlinear regime (input laser power of 520 mW) for different rotational speeds (Ω) in units of deg/s. At low speeds, trajectories are significantly distorted and have paths similar to the 100 mW results, but with more distortion due to stronger nonlinear coupling between beams. At high speeds, the coupling between beams is weaker due to the finite response time of the medium. For slow speeds $\Omega \leq 100$, the trajectories are very noisy, and no discernable pattern is easily observed. This behavior is mainly due to the thermal gradient impressed on the crystal by intense illumination, and therefore, the transverse beam shape is drastically modified.

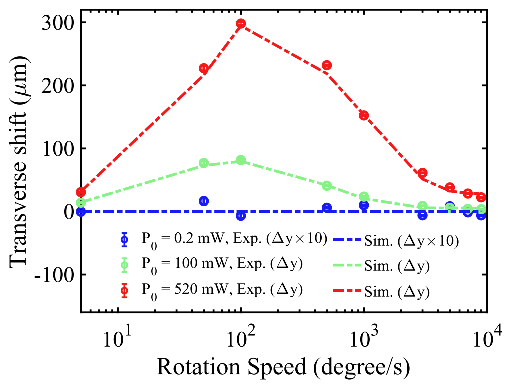

Fig. 6. Experimental and simulated amount of shift in the beam's transverse position at the end of the crystal for 0.2, 100, and 520 mW input beam laser power. The measured shift for the linear regime (i.e., $P_0 = 0.2$ mW) for both experiment and simulations is multiplied by a factor of 10, showing that there is no discernible deviation from zero shift. The magnitude of the transverse shift is shown against the magnitude of the rotation speed. This shift is calculated between the position with no rotation, i.e., $\Omega = 0$ deg/s, and the respective transversely shifted position. Simulations are plotted using dotted lines in green and red for nonlinear and highly nonlinear regimes, respectively, for better comparison to experimental data. The fits were based on a phenomenological exponential function in Eq. (2). The fit is not a perfect match due to the simulated nonlinear response of the material acting on the beams upon propagation through the crystal.

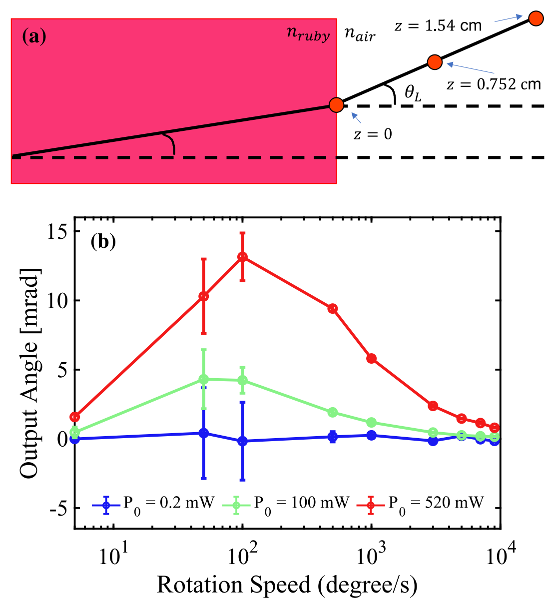

Fig. 7. (a) Schematic showing the output beam's angle after leaving the crystal. The nonlinear response of the crystal changes the angle at the interface of the crystal output face and therefore changes the propagation pathway. (b) The output angle and its uncertainty are calculated from the beams' transverse positions measured at three points along the z axis ($z = 0$, z = 0.762, and $z = 1.524$ cm). As the laser's power increases, the output angle increases as expected from nonlinear deflection.

We extract the average position of these COI trajectories over an integer number of full rotations. Figure 6 shows the rotation speed dependence of the extracted transverse shift at $z = 0$ (crystal's output face) for linear, nonlinear, and highly nonlinear regimes. While there is no clear transverse shift in the linear regime, the nonlinear regimes show a trend similar to that of a log-normal function centered around $\Omega = 100$ deg/s. Therefore, the observed transverse shift is a purely nonlinear effect.

We note that the transverse spatial shift can, in principle, comprise nonlinear photon-drag and nonlinear deflection. While the photon-drag transversely shifts the beam with an output parallel to the input beam, the nonlinear deflection deflects the output beam at an angle with respect to the input. Therefore, to discriminate these two effects, we measure the transverse shifts at $z = 0$ and two other locations after the crystal to find the output angle. It is important to note that we cannot subtract out the deflection to get the true shift due to the photon-drag effect. The changes in the trajectory inside the crystal by nonlinear deflection cannot be imaged. As expected from nonlinear deflection, this angle is nonzero and intensity and rotation speed dependent (Fig. 7).

4. DISCUSSION

A. Nonlinear Refraction

Intense linearly polarized light in a rotating birefringent medium causes o- and e-beams to both experience nonlinear refraction, as the maximum intensity continuously moves between them creating a moving index gradient. The gradient leads to nonlinear coupling between beams, where the local index variation pulls one beam toward the other with the higher refractive index, locally distorting the figure-eight-like COI trajectory. The magnitude of the distortions is dictated by the rotation speed, where the speed controls the amount of time that the beam imprints an index gradient on the crystal. The maximum strength of beam coupling is observed at low speeds when the beams have sufficient time to imprint the maximum nonlinear index. On the contrary, higher rotation speeds imprint less gradient, blurring the effect of nonlinear refraction, and non-distorted figure-eight-like trajectories are recovered.

The speed regimes highlight different interaction time scales of the nonlinear response. Both optical and thermal processes are relevant; however, thermal processes dominate at slow speeds and optical at high speeds. Since the time scale of thermal processes is of the order of several hundred microseconds [42], this would have a greater effect locally with slower rotation speeds. However, we examine the effects over a complete cycle, and therefore, high rotation speeds are affected more by optical time scales, which in our case are of the order of 3–5 ms.

We model the temporal dynamics in these two regimes using a phenomenological fit consisting of two decaying exponentials discussed later in this paper where we take an analogy to spatial self-steepening [43,44]. That is, the beam is shifted due to the group index, and therefore the group velocity, which is intensity and rotation speed dependent. This rotation speed dependence therefore samples the dynamics representing a non-instantaneous temporal response of the system.

This behavior could be considered an effective time-varying response. Time-varying media often rely on highly nonlinear materials, such as epsilon-near-zero materials [45], that change the refractive index in time [46,47], inviting optical effects such as non-reciprocity [48,49]. The strong nonlinear optical response of ruby could perhaps exhibit non-reciprocity due to an effective time-varying effect, but further work needs to be done. The magnitude of the index gradient induced by nonlinear refraction ($\Delta n = 3 \times 10^{-3}$) is shown in Supplement 1, as well as its use in the formation of a Townes profile in the steady-state, stationary medium case.

B. Simulations

To better understand the experimental results, we model and simulate nonlinear propagation of linearly polarized light through a 2 cm long rotating birefringent ruby rod, where o- and e-beams are created and vary in relative intensity upon rotation. Due to the weak birefringence typically associated with ruby and intense illumination, these two beams couple to each other upon rotation. Both beams are modeled using the nonlinear Schrödinger equation where we apply a split-step Fourier method and propagate the two with a coupling term containing a nonlinear response function. Following the derivation of Marcucci *et al.* [50], we write wave equations for the medium using a Kerr-type nonlinearity of thermal origin. Rotation and birefringence are also included [51]. Furthermore, a term for the effective group index is incorporated into the coupled equations, which are intensity and rotation speed dependent.

Using our theoretical framework, including the phenomenological fit convoluted with nonlinear propagation, we were able to accurately simulate the amount of transverse shift, and the transverse movement of the COI of the beams observed in the experiment. We develop a set of generalized coupled nonlinear Schrodinger equations, written as follows:

$$-\frac{\partial E_o}{\partial z} + \frac{i}{2k_o}\nabla_\perp^2 E_o + \left(n_g^{\text{eff}}\frac{\partial E_o}{\partial y} + \frac{ik_o}{n_o}\Delta n_{\text{NL}} E_o\right) = 0, \quad (3)$$

$$\begin{aligned} &-\frac{\partial E_e}{\partial z} + \frac{i}{2k_e\cos^2(\gamma)}\nabla_\perp^2 E_e \\ &+\left(\frac{ik_e}{n_e\cos^2(\gamma)}\Delta n_{\text{NL}} E_e + n_g^{\text{eff}}\frac{\partial E_e}{\partial y}\right) \\ &+2\tan(\gamma)\left[\cos(\Omega t)\frac{\partial E_e}{\partial x} + \sin(\Omega t)\frac{\partial E_e}{\partial y}\right] = 0, \end{aligned} \quad (4)$$

where fields E_o and E_e represent o- and e- beams, $k_{o,e}$ are o- and e-beam wave vectors, and $n_{o,e}$ are o- and e-beam refractive indices, respectively. Furthermore, γ is the tilt angle, $\nabla_\perp^2 = \frac{\partial^2}{\partial x^2} + \frac{\partial^2}{\partial y^2}$ is the transverse Laplacian operator, and Δn_{NL} is the nonlocal Kerr-type nonlinearity that contains the coupling term in the kernel function [50]. We also highlight that the nonlinear deflection term works on the derivative of the field rather than the field directly like that of nonlinear refraction. Dispersion is also included in the nonlinear Schrodinger equation; however, this effect is written as $n_g^{\text{eff}}\frac{\partial E}{\partial y}$ rather than $n_g^{\text{eff}}\frac{\partial E}{\partial t}c^{-1}$, when considering a CW laser rather than pulses. This term will drive the nonlinear deflection measured at the crystal output face, where $n_g^{\text{eff}} := n_g^{\text{eff}}(\Omega, I)$, as in Eq. (7).

The magnitude of the nonlinear deflection is proportional to the magnitude of the effective group index, controlled by the intensity and rotation speed. The rotation speed changes the conditions for how quickly heat dissipates through the crystal, and thus the magnitude of the index gradient. If the speeds are sufficiently slow, the index gradient stays relatively constant and causes an increasing amount of transverse shift. Typically, the time scale needed to deflect the beam is always very short [i.e., 2 cm$/(c/n_g)$]; however, once the maximum amount of transverse shift is met, i.e., $\Omega \approx 100$ deg/s, the crystal starts rotating faster than the time scale needed to form the index gradient. As we increase the rotation speed, the beam sees less index gradient and thus less transverse shift. The curve associated with the transverse shift versus rotation speed, seen in Fig. 6, comprises two decaying exponentials centered about $\Omega = 100$ deg/s. The decay rates of these two exponentials give rise to an asymmetric distribution about $\Omega = 100$ deg/s. For slow speeds, the index gradient decays slower and does not blur. At higher speeds, the beam samples only some of the index gradient due to the shorter time scale of the rotational motion and is therefore smaller in magnitude. This is shown in Fig. 6, where the behavior is not symmetric about $\Omega = 100$ deg/s.

We draw an analogy to a self-steepened pulse to explain the asymmetry of the transverse shift versus rotation speed. In a self-steepened pulse, the group velocity travels at different speeds dependent on the intensity. As such, different parts of the pulse travel at speeds according to the group velocity. Higher intensities seen at the peak of the pulse are associated with a large group index and thus slower group velocity. At the wings of the pulse, the intensity is lower and the group velocity is larger. This causes the pulse to become asymmetric in time, and thus the material response will be temporally asymmetric. The rotation speed controls the amount of time that maximum intensity is in a given area, and therefore, the index gradient will be temporally asymmetric. As a result, the amount of transverse shift will also change asymmetrically.

A phenomenological fit for the transverse shift was created using the experimental data in Fig. 6 with the form of a decaying exponential (see Supplement 1). Thus, we can represent the maximum imprinted nonlinear group index as $\Delta n_g = n_2^g I_{\max}(t) = n_2^g I_0 \exp(-t/\tau_c)$, where I_0 is the input intensity, and τ_c is a characteristic decay time of the nonlinear response, which we ascribe to thermal diffusion as the dominant thermal contribution to the nonlinear response. Let us write the time in terms of the rotation speed as $t = \tau_c \Omega/\Omega_c$, where Ω is the rotation speed, Ω_c is a characteristic rotation speed, and we rewrite the transverse shift to be

$$\Delta y \approx \frac{r \Omega L n_g^{\text{eff}}}{c}, \tag{5}$$

where n_g^{eff} is the effective group index written as

$$n_g^{\text{eff}} = n_g^0 + n_2^g I = n_g^0 + n_2^g I_o e^{-\Omega/\Omega_c}. \tag{6}$$

We can look at the time-average response of the effective group index for a given speed. For a given speed, average temporal response can be broken up into a fast and slow contribution written as

$$n_g^{\text{eff}} = n_g^0 + n_2^g I_o \left(\frac{1}{f_s} e^{-\Omega/\Omega_s} - f_f e^{-\Omega/\Omega_f} \right), \tag{7}$$

where $n_2^g I_o = 10^7$, and f_s and f_f are scaling factors equal to 0.97 and 0.94, respectively. These values are similar to those when considering the peak power of a Gaussian pulse. Ω_s and Ω_f refer to the slow and fast inverse time scales, where $\Omega_{s,f} = 1/(2\pi \tau_{s,f})$, and the slow and fast time scales are $\tau_s = 3.5$ ms and $\tau_f = 175$ µs, respectively. The slow (optical) time scale is of the order of the excited ion lifetime, typically 3 to 5 ms [26], and the fast (thermal) time scale is of the order of thermal diffusion (≈ 200 µs) [42]. Equation (7) can be seen plotted in Supplement 1.

Fast and slow time scales modify the magnitude of the effective group index, representing an approximate non-instantaneous response. The nonlinear response of the medium is indeed non-instantaneous, but this approach represents, to a good approximation, the dynamics of the system while alleviating computational expense when one includes a non-instantaneous response in the simulations. Equation (7) is then introduced into a generalized nonlinear Schrödinger equation, and nonlinear propagation is simulated to investigate the transverse COI trajectories and extract the amount of transverse shift. These results are shown in Figs. 3–5, achieving good agreement among the trajectories and the transverse shift due to photon-drag and nonlinear deflection.

From Eqs. (3) and (4), we represent the static nonlinear refraction as an index gradient of the form

$$\Delta n_{\text{NL}}(x, y, \Omega t, \gamma) = n_2 \iint \mathrm{d}\tilde{x}\mathrm{d}\tilde{y} K_\gamma \left(\Delta x, \Delta y, \Omega t\right) I(\tilde{x}, \tilde{y}) - n_{o,e}, \tag{8}$$

where $\Delta x = x - \tilde{x}$, and $\Delta y = y - \tilde{y}$. Here, $\tilde{x}$ and $\tilde{y}$ are Cartesian coordinates of an arbitrary position within the space where the nonlinear kernel function acts. The nonlinear potential in the laboratory's frame depends on the crystal's response function K' [50], which is given by the thermal properties of the material:

$$K_\gamma \left(x, y, \Omega t\right)/K' = \left[\cos(\gamma)\cos(\Omega t)x + \cos(\gamma)\sin(\Omega t)y, -\sin(\Omega t)x + \cos(\Omega t)y\right], \tag{9}$$

and $I = |E_o|^2 + |E_e|^2$.

A further explanation of the theoretical modeling of light propagation through a moving nonlinear medium is discussed by Hogan *et al.* [52]. Upon propagating two beams through the crystal, we extract two main parameters as a function of the input intensity and rotation speed: (1) the position of the COI in the transverse plane and (2) the transverse shift (overall average position of the COI trajectories) experienced by the beams at the output face of the crystal. The COI trajectories and the values of the transverse shift are determined for a variety of crystal rotation speeds, and the three powers used in the experiment with the addition of the phenomenological fit in the drift term as a modified effective group index. Results of the simulations are presented in Figs. 3–5 for direct comparison to experimental data.

It is important to note that by moving the camera closer to the crystal, one can image the input face of the crystal at which a seemingly negative drag is observed, i.e., the beams appear to be shifted in directions opposite to the motion of the crystal. However, we highlight that such a measurement simply extrapolates the output beams toward the input face of the crystal and leads to a seemingly negative drag effect as a consequence of the large output angle due to nonlinear deflection.

When the medium response is not instantaneous, the imprinted refractive index profile is dragged along with the medium motion. The light then interacts with this moving index gradient and is therefore deflected at an angle. For example, in a typical nonlinear interaction with a positive nonlinear refractive index, i.e., self-focusing, the beam deflects toward the direction of medium motion and thus resembles a positive photon-drag effect. However, the output beam leaves the moving medium at an angle with respect to the input beam. Therefore, in any measurement of the transverse drag effect, it is crucial to measure the output angle to discriminate the photon-drag effect from any beam deflection.

5. CONCLUSION

We have demonstrated experimentally and through simulation that a 2 cm long rotating ruby crystal illuminated with 473 nm light produces a transverse shift as a result of nonlinear photon-drag and nonlinear deflection. In rotating saturable media with self-focusing nonlinear refraction, one must measure the output angle to distinguish nonlinear deflection and transverse photon-drag. We note that even if the medium presents large negative group indices, nonlinear deflection can dominate negative drag when nonlinear refraction is large and positive. The maximum transverse shift is found to be $\Delta y = +300$ µm, and the maximum angular shift is found to be $\theta = 13$ mrad at the output face of the crystal ($z = 0$). Moreover, exotic trajectories were observed experimentally for the COI of the beam in the transverse plane at the crystal output face and reproduced in simulation with good agreement. Since the position of the transverse profile of the beam is controllable by the rotation speed of the crystal and input intensity of the beam, one can imagine applications in beam steering and image rotation, velocimetry, as well as understanding the resilience of the state of polarization to the motion of the medium.

Funding. Natural Sciences and Engineering Research Council of Canada (PDF-546105-2020, RGPIN/2017-06880, Banting Postdoctoral Fellowship); Canada Research Chairs (950-231657); Canada First Research Excellence Fund (072623); Office of Naval Research (N00014-19-1-2247); North Shore Micmac District Council's (NSMDC) Post-Secondary Education Program; Multidisciplinary University Research Initiative (N00014-20-1-2558).

Acknowledgment. The authors thank Xiaoqin Gao for valuable advice on making figures and the structural formatting of the manuscript. The authors also thank Orad Reshef for his insightful comments on the manuscript. R.W.B. and R.H. acknowledge support through the NSERC, the Canada Research Chairs program, and the Canada First Research Excellence Fund on Transformative Quantum Technologies. In addition, R.W.B. acknowledges support through the U.S. Office of Naval Research. R.H. acknowledges support through Indigenous Affairs at the North Shore Micmac District Council. A.S. acknowledges the support of NSERC. B.B. also acknowledges the support of the Banting postdoctoral fellowship of NSERC. A.S. conceived the experiment, R.H. and A.S. conducted the experiment, R.H. and B.B. analyzed the results, G.M. and R.H. developed the theory and conducted simulations, R.H. wrote the article and R.W.B. supervised this work. All authors reviewed the manuscript.

Disclosures. The authors declare no conflicts of interest.

Data availability. Readers may email the corresponding author, Ryan Hogan, for any code that may be needed for their purpose. He can be contacted at rhoga054@uottawa.ca. We will respond to reasonable requests for the code.

Supplemental document. See Supplement 1 for supporting content.

REFERENCES

1. A. Fresnel, "Lettre d'augustin fresnel à françois arago sur l'influence du mouvement terrestre dans quelques phénomènes d'optique," Ann. Chim. Phys. **9**, 57–66 (1818).
2. M. H. Fizeau, "XXXII. On the effect of the motion of a body upon the velocity with which it is traversed by light," Philos. Mag. **19**(127), 245–260 (1860).
3. N. L. Balazs, "The propagation of light rays in moving media," J. Opt. Soc. Am. **45**, 63–64 (1955).
4. W. F. Parks and J. T. Dowell, "Fresnel drag in uniformly moving media," Phys. Rev. A **9**, 565 (1974).
5. U. Leonhardt and P. Piwnicki, "Slow light in moving media," J. Mod. Opt. **48**, 977–988 (2001).
6. M. Artoni, I. Carusotto, G. C. La Rocca, and F. Bassani, "Fresnel light drag in a coherently driven moving medium," Phys. Rev. Lett. **86**, 2549 (2001).
7. J. B. Götte, S. M. Barnett, and M. Padgett, "On the dragging of light by a rotating medium," Proc. R. Soc. A **463**, 2185–2194 (2007).
8. I. Carusotto, M. Artoni, G. C. La Rocca, and F. Bassani, "Transverse Fresnel-Fizeau drag effects in strongly dispersive media," Phys. Rev. A **68**, 063819 (2003).
9. U. Leonhardt and P. Piwnicki, "Relativistic effects of light in moving media with extremely low group velocity," Phys. Rev. Lett. **84**, 822 (2000).
10. A. Khan, S. A. Ullah, M. S. Abdul Jabar, and B. A. Bacha, "Fizeau's light birefringence dragging effect in a moving chiral medium," Eur. Phys. J. Plus **136**, 1–13 (2021).
11. T. Qin, J. Yang, F. Zhang, Y. Chen, D. Shen, W. Liu, L. Chen, X. Jiang, X. Chen, and W. Wan, "Fast-and slow-light-enhanced light drag in a moving microcavity," Commun. Phys. **3**, 1–8 (2020).
12. R. Y. Chiao, E. Garmire, and C. H. Townes, "Self-trapping of optical beams," Phys. Rev. Lett. **13**, 479 (1964).
13. G. Fibich and A. L. Gaeta, "Critical power for self-focusing in bulk media and in hollow waveguides," Opt. Lett. **25**, 335–337 (2000).
14. G. Meyer and N. M. Amer, "Optical-beam-deflection atomic force microscopy: the NaCl (001) surface," Appl. Phys. Lett. **56**, 2100–2101 (1990).
15. P. B. Dixon, D. J. Starling, A. N. Jordan, and J. C. Howell, "Ultrasensitive beam deflection measurement via interferometric weak value amplification," Phys. Rev. Lett. **102**, 173601 (2009).
16. A. F. Gibson, M. F. Kimmitt, and A. C. Walker, "Photon drag in germanium," Appl. Phys. Lett. **17**, 75–77 (1970).
17. J. H. Yee, "Theory of photon-drag effect in polar crystals," Phys. Rev. B **6**, 2279 (1972).
18. A. F. Gibson and M. F. Kimmitt, "Photon drag detection," in *Infrared and Millimeter Waves*, Vol. **3** (Academic, 1980), pp. 181–217.
19. A. A. Grinberg and S. Luryi, "Theory of the photon-drag effect in a two-dimensional electron gas," Phys. Rev. B **38**, 87 (1988).
20. A. D. Wieck, H. Sigg, and K. Ploog, "Observation of resonant photon drag in a two-dimensional electron gas," Phys. Rev. Lett. **64**, 463 (1990).
21. D. Strekalov, A. B. Matsko, N. Yu, and L. Maleki, "Observation of light dragging in a rubidium vapor cell," Phys. Rev. Lett. **93**, 023601 (2004).
22. S. Davuluri and Y. V. Rostovtsev, "Controllable enhanced dragging of light in ultradispersive media," Phys. Rev. A **86**, 013806 (2012).
23. S. H. Kazemi and M. Mahmoudi, "Phase-controlled photon drag in a slow-light moving medium," arXiv, arXiv:1810.00560 (2018).
24. R. V. Jones, "'Aether drag' in a transversely moving medium," Proc. R. Soc. Lond. A **345**, 351–364 (1975).
25. A. Safari, I. De Leon, M. Mirhosseini, O. S. Magaña-Loaiza, and R. W. Boyd, "Light-drag enhancement by a highly dispersive rubidium vapor," Phys. Rev. Lett. **116**, 013601 (2016).
26. S. Franke-Arnold, G. Gibson, R. W. Boyd, and M. J. Padgett, "Rotary photon drag enhanced by a slow-light medium," Science **333**, 65–67 (2011).
27. M. S. Bigelow, N. N. Lepeshkin, and R. W. Boyd, "Superluminal and slow light propagation in a room-temperature solid," Science **301**, 200–202 (2003).
28. L. V. Hau, S. E. Harris, Z. Dutton, and C. H. Behroozi, "Light speed reduction to 17 metres per second in an ultracold atomic gas," Nature **397**, 594–598 (1999).
29. C. Banerjee, Y. Solomons, A. Nicholas Black, G. Marcucci, D. Eger, N. Davidson, O. Firstenberg, and R. W. Boyd, "Anomalous optical drag," Phys. Rev. Res. **4**, 033124 (2022).
30. J. S. Toll, "Causality and the dispersion relation: logical foundations," Phys. Rev. **104**, 1760 (1956).
31. R. V. Jones, "'Fresnel aether drag' in a transversely moving medium," Proc. R. Soc. Lond. A **328**, 337–352 (1972).
32. J. Leach, A. J. Wright, J. B. Götte, J. M. Girkin, L. Allen, S. Franke-Arnold, S. M. Barnett, and M. J. Padgett, "'Aether drag' and moving images," Phys. Rev. Lett. **100**, 153902 (2008).
33. A. Safari, C. Selvarajah, J. Evans, J. Upham, and R. W. Boyd, "Strong reverse saturation and fast-light in ruby," arXiv, arXiv:2301.13300 (2023).
34. L. Boccia, I. Russo, G. Amendola, and G. Di Massa, "Tunable frequency-selective surfaces for beam-steering applications," Electron. Lett. **45**, 1213–1215 (2009).
35. I. Golub, "Beam deflection and ultrafast angular scanning by a time-varying optically induced prism," Opt. Commun. **94**, 143–146 (1992).
36. R. D. Allen, J. Brault, and R. D. Moore, "A new method of polarization microscopic analysis: I. scanning with a birefringence detection system," J. Cell Biol. **18**, 223–235 (1963).
37. J.-Q. Gong, H.-G. Zhan, and D.-Z. Liu, "A review on polarization information in the remote sensing detection," Spectrosc. Spectral Anal. **30**, 1088–1095 (2010).
38. R. J. Adrian, "Twenty years of particle image velocimetry," Exp. Fluids **39**, 159–169 (2005).
39. A. Hasegawa, "An historical review of application of optical solitons for high speed communications," Chaos **10**, 475–485 (2000).
40. M. J. Ablowitz, G. Biondini, and L. A. Ostrovsky, "Optical solitons: perspectives and applications," Chaos **10**, 471–474 (2000).
41. Y. S. Kivshar and B. Luther-Davies, "Dark optical solitons: physics and applications," Phys. Rep. **298**, 81–197 (1998).
42. S. Doiron and A. Haché, "Time evolution of reflective thermal lenses and measurement of thermal diffusivity in bulk solids," Appl. Opt. **43**, 4250–4253 (2004).
43. J. R. De Oliveira, M. A. de Moura, J. M. Hickmann, and A. S. L. Gomes, "Self-steepening of optical pulses in dispersive media," J. Opt. Soc. Am. B **9**, 2025–2027 (1992).
44. S. M. Hernández, J. Bonetti, N. Linale, D. F. Grosz, and P. I. Fierens, "Soliton solutions and self-steepening in the photon-conserving nonlinear Schrödinger equation," Waves Random Complex Medium **32**, 2533–2549 (2020).
45. Y. Zhou, M. Zahirul Alam, M. Karimi, J. Upham, O. Reshef, C. Liu, A. E. Willner, and R. W. Boyd, "Broadband frequency translation through time refraction in an epsilon-near-zero material," Nat. Commun. **11**, 2180 (2020).
46. E. Galiffi, R. Tirole, S. Yin, H. Li, S. Vezzoli, P. A. Huidobro, M. G. Silveirinha, R. Sapienza, A. Alù, and J. B. Pendry, "Photonics of time-varying media," Adv. Photon. **4**, 014002 (2022).
47. S. Taravati, "Giant linear nonreciprocity, zero reflection, and zero band gap in equilibrated space-time-varying media," Phys. Rev. Appl. **9**, 064012 (2018).

48. C. Caloz, A. Alu, S. Tretyakov, D. Sounas, K. Achouri, and Z.-L. Deck-Léger, “Electromagnetic nonreciprocity,” Phys. Rev. Appl. **10**, 047001 (2018).
49. S. Manipatruni, J. T. Robinson, and M. Lipson, “Optical nonreciprocity in optomechanical structures,” Phys. Rev. Lett. **102**, 213903 (2009).
50. G. Marcucci, D. Pierangeli, S. Gentilini, N. Ghofraniha, Z. Chen, and C. Conti, “Optical spatial shock waves in nonlocal nonlinear media,” Adv. Phys. X **4**, 1662733 (2019).
51. C. Conti, M. Peccianti, and G. Assanto, “Spatial solitons and modulational instability in the presence of large birefringence: the case of highly nonlocal liquid crystals,” Phys. Rev. E **72**, 066614 (2005).
52. R. Hogan, G. Marcucci, A. Safari, N. A. Black, B. Braverman, J. Upham, and R. W. Boyd, are preparing a manuscript to be called, “Modelling nonlinear propagation effects on beam deflection and negative drag,” (2023).